# Effect of organic nano-components on the thermoelectric properties of Sb2Te3 nanocrystal thin film

M. Wei, T.-B. Chen, J.-G. Hu, S. Chen, H.-L. Ma, J.-T. Luo, G.-X. Liang, X.-H. Zhang, P. Fan, Z.-H. Zheng

# Effect of organic nano-components on the thermoelectric properties of $Sb_2Te_3$ nanocrystal thin film

Meng Wei [a,b], Tian-bao Chen [a,b], Ju-guang Hu [a], Shuo Chen [a], Hong-li Ma [b], Jing-ting Luo [a], Guang-xing Liang [a], Xiang-hua Zhang [b], Ping Fan [a], Zhuang-hao Zheng [a,*]

a Shenzhen Key Laboratory of Advanced Thin Films and Applications, College of Physics and Optoelectronic Engineering, Shenzhen University, Shenzhen 518060, China

b Laboratory of Glasses and Ceramics, Univ Rennes, CNRS, ISCR( Institut des Sciences Chimiques de Rennes) UMR CNRS 6226, University of Rennes 1, Rennes 35042, France.

* Corresponding author. E-mail: zhengzh@szu.edu.cn

**Abstract** In this work, organic $CH_3NH_3I$ nano-components were successfully introduced into $Sb_2Te_3$ nanocrystal thin film via using the layer-by-layer evaporation growth method. The thermoelectric properties, including the electrical conductivity, Seebeck coefficient, thermal conductivity and the estimated figure of merit were investigated. The experimental results indicated that the introduced organic nano-components are beneficial to improving the Seebeck coefficient of the $Sb_2Te_3$ nanocrystal thin film, resulting in over 100% enhancement of figure of merit. These results prove our hypothesis that the organic hybrid can greatly enhance the thermoelectric property of the $Sb_2Te_3$ thin film based on the energy-filtering effect.

**Keywords** Thermoelectric materials; Thin films; Organic; Inorganic

Thermoelectric (TE) materials can directly convert heat into electricity and vice versa, which have the unique advantage of providing a clean, quiet, reliable and safe source of power generation or solid-state cooling [1, 2]. Recently, thin film TE materials are widely studied due to their great potential in fabricating micro-size, light weight and flexible device that can be used in self-powered or wearable microelectronic applications [3, 4]. The performance of TE material is mainly gauged by two common indicators, dimensionless figure of merit, $ZT=S^2\sigma T/\kappa$, and power

factor, $PF=S^2\sigma$, where $S$, $\sigma$, T and $\kappa$ are the Seebeck coefficient, electrical conductivity, absolute temperature and total thermal conductivity from electron ($\kappa_{ele}$) and phonon ($\kappa_{lat}$) contributions [5]. In order to enhance $ZT$, the Seebeck coefficient, electrical conductivity and thermal conductivity should be optimized; however, these parameters are strongly interrelated with carrier concentration, making difficult to increase one parameter without effect on the others [6]. Nano-structure strategy is an efficient way to break these relationships in bulk TE materials that allow for improved thermoelectric performance due to more severe thermal conductivity resistances than electric [7-9]. Indeed, significant enhancement in both $PF$ and $ZT$ has also been realized in thin film TE materials by adopted nono-structure such as superlattice and nano-crystals [10, 11]. However, it remains a significant challenge to implement these approaches due to the complex fabrication processes [12].

Antimony telluride ($Sb_2Te_3$) based materials have intrinsic excellent thermoelectric performance around room temperature [13, 14] and they have been widely employed for preparing thin film TE materials by using various methods, including magnetron sputtering [15], co-evaporation [16], pulsed laser deposition [17], screen printing [18], solution process [19]. However, despite some improvement of TE performance realized by preparing parameters optimization, the $Sb_2Te_3$ based thin films usually exhibit the lower $PF$ or $ZT$ value than that of the bulk form [20-22]. Recently, a series of remarkable researches showed that inorganic-organic hybrid can greatly enhanced the TE performance of the materials [23-25], providing another efficient way for further improving the TE performance of the thin films. For instance, Hyun Ju et al. [26] and Wang et al. [27] developed inorganic/poly (3,4-ethylenedioxythiophene): poly (styrene sulfonate) nanocomposites thin films and shown ultrahigh $PF$ value due to the great enhancement of Seebeck coefficient by energy filtering effect. On the other hand, hybrid thin films also have lower thermal conductivity than that of fully inorganic material, which attribute to the larger phonon scattering due to the introduced nano-inclusions and organic-inorganic grain interfaces [28-30].

Organic $CH_3NH_3I$ has been studied in different fields; especially in photovoltaic because of its outstanding optical, magnetic, and electronic properties [31-33]. It

might have great potential as an benefit organic component for preparing high-performance hybrid $Sb_2Te_3$ based thin film since, (i) crystalline $CH_3NH_3I$-based materials show excellent electrical transport characteristic thanks to the high carrier mobility, which is beneficial for thermoelectric materials to obtain more superior thermoelectric properties; (ii) it can provide considerable iodine ions to promote the crystallization and growth of the inorganic crystals which has been reported that the iodine can effectively enhance the TE properties of Sb based bulk materials by acting as nucleating agent during the crystallization process, and (iii) The nano-size organic component diffused around the grain boundary can create more scattering centers and scattered wide range of phonons, leading to reduce the thermal conductivity. Herein, in the present work, $CH_3NH_3I$ was employed to fabricate inorganic-organic nano-composites $Sb_2Te_3$ based thin film through the layer-by-layer evaporation growth method. Results show that the Seebeck coefficient of the $Sb_2Te_3$ thin film has greatly enhanced together with the decreased of thermal conductivity after $CH_3NH_3I$ hybrid, resulting in about 100% enhancement of figure of merit.

The organic $CH_3NH_3I$ is prepared by conventional method and the details are below: Methylammonium iodide (MAI) was synthesized by using 28 milliliter (ml) methylamine ($CH_3NH_2$) (Sigma Aldrich) and 30 ml hydroiodic acid (HI) (Sigma Aldrich), which were 57 wt% and 40 wt% in water respectively. Then put them in an ice bath device with a 250 ml flask at 0 °C under constant magnetic stirring for 2 hours. After that, transfer the reaction mixture to the beaker, which is placed in the heated water at the constant temperature of 95°C, until the white powder of $CH_3NH_3I$ is obtained. The purification process carried out with diethyl ether three times. The high purity crystallized white methylammonium iodide (MAI) powder was obtained after drying at 60 °C in a vacuum chamber over ten hours.

High-purity $Sb_2Te_3$ powder (99.99%, purchase from Aladdin) and the prepared $CH_3NH_3I$ powder were placed in two thermal evaporators (Tungsten evaporation boat) respectively. K7 glass substrate was used for depositing thin film, which was cleaned with acetone, alcohol, and deionized water for 15 min followed by drying with $N_2$ gas. Then, argon of high purity is pumped into the vacuum chamber and the operating

pressure is $2.1\times10^{-3}$ Pa. Fig.1 shows the thin film deposition process. Firstly, the precursor $Sb_2Te_3$ thin film was prepared onto the glass substrate for 10 min using the evaporation current of 120 A. Then the $CH_3NH_3I$ layer was evaporated for 5 min onto the prepared $Sb_2Te_3$ layer by using evaporation current of 80 A. After that, the $Sb_2Te_3$ thin film was deposited with same condition of the precursor $Sb_2Te_3$ thin film. Finally, the $Sb_2Te_3/CH_3NH_3I/Sb_2Te_3$ multilayer was taken an in situ annealing process at 448 K for 1 hour under an Ar atmosphere.

The crystal structure of the films was measured by X-ray diffraction (XRD) (D/max-2500, Rigaku Corporation) in θ-2θ mode (Cu/Ka radiation (40 kV)). The surface morphology and composition were characterized by scanning electron microscopy (SEM, Zeiss supra 55) by using an energy dispersive X-ray spectrometer system, attached with an energy dispersive X-ray spectrometer (EDS) system. Raman scattering measurements were performed with the equipment (Renishaw inVia), which the laser excitation was 514.5 nm line of an $Ar^+$ ion laser. Transmission electron microscopy (TEM) (JEM-3200FS) with energy dispersive spectroscopy (EDS), used to characterize the micro-structure and component analyses of the thin film. The electrical conductivity and the Seebeck coefficient were measured by the thermoelectric performance test system (SBA458 Netzsch). The carrier mobility and concentration were measured by using the Hall measurement system (HL5500PC, Nanometrics) at room temperature. The room temperature thermal conductivity was measured with transient hot-wires theory method [31].

EDS analysis was performed to identify the Sb, Te and I atomic contents of the thin films, and the result is shown in Table 1. The Sb to Te atomic ratio of the pristine $Sb_2Te_3$ thin film is 40.1:59.9, indicating the stoichiometric content. It has slightly decreased after $CH_3NH_3I$ hybrid and demonstrated a little Sb-rich with the I atomic content of 0.5 %. The hall measurements of the thin films were also listed in Table 1. It can be seen that the carrier concentration decreases and carrier mobility increases after $CH_3CH_3I$ hybrid.

Fig. 2(a) presents the XRD patterns of the pristine and hybrid thin films. The same phases corresponding to the $Sb_2Te_3$ without impurity peak are observed from these

two patterns, indicating the samples have single $Sb_2Te_3$ crystal and well crystallinity. However, the (006), (015) and (1010) plane peaks of the pristine sample are the strongest, and changes to the preferential orientations of (015) and (110) planes of the hybrid thin film, suggesting the organic component has a significant effect on the thin film crystal growth. The surface morphologies are also investigated some difference between the pristine and hybrid thin films as shown from the SEM images inserted in the right side of Fig.2a. The hexagonal-liked surface structure is obtained from the pristine thin film which is the typical structure of $Sb_2Te_3$ [14]. Differently, a smooth surface containing large domains from the nanocrystal clusters together after $CH_3NH_3I$ hybrid. This containing nanocrystal structure might lead to a high TE performance. However, it cannot find any related peak related to the $CH_3NH_3I$ or I from the XRD and SEM results. So to further confirm the status of organic components in the hybrid thin film, Raman analysis was taken as shown in Fig. 2(b). Based on the theoretical calculation [34], there are four Raman sensitive phonon vibration modes for $Sb_2Te_3$ single crystal in the range of 40 $cm^{-1}$ to 255 $cm^{-1}$, identified as $2A_{1g} + 2E_g$ [35]. Here, three typical $Sb_2Te_3$ Raman modes are visible that located at 68.2 $cm^{-1}$, 119.7 $cm^{-1}$ and 165.4 $cm^{-1}$, corresponding to the $A^1_{1g}$, $E^2_g$ and $A^2_{1g}$, respectively. Interestingly, another three Raman peaks are matched to the characteristic peaks of $CH_3NH_3I$ [36], indicating that both of the $Sb_2Te_3$ and $CH_3NH_3I$ crystallites exist in the composited thin film.

TEM results were shown in Fig. 2(c)~(g). Fig. 2(c) shows distinct composited thin film which performed by FEI (scios). The picture is divided into three parts, Pt (The portion left when preparing a sample), composite film, and substrate. The area marked in yellow was analyzed with high resolution, shown in Fig. 2(d) and Fig 2(e). The distinct grain boundary marked by the yellow dotted line, and obvious distribution of amorphous and grain regions can also be observed. But they grow laterally along different axis due to the introduction of organic functional groups. Based on the analysis above, it can be inferred that organic component are located in the middle of the composited structure, due to the limited diffusion and deficiency of the organic component in the composited structure. This result shows that inorganic atoms are

crystallized under the adsorption of organic functional groups and the iodine ions act as nucleating and catalyst component. With the annealing process, the grains are grown under organic functional groups and the iodine ions, and also have more iodine ions diffusion, even if most of organic functional groups component are located in the middle of the composited structure. Fig. 2(f) and (e) shows that the full scale counts patterns which were point 1 and 2 from (d).It can be seen that the point 1 is rich in Sb and Te element, and it contains a small amount of I. It indicates that $Sb_2Te_3$ is the main component in this region, while other doping content is slight. As the Fig. 2(e) shown, Sb and Te are also abundant near point 2, but the content of them were lower than that at point 1, the content of I act the same situation as them. It demonstrated that iodide was indeed dispersed to other layers, while the content of C was higher than that at point 1. Therefore, it could be inferred that most organic functional groups remained in the middle layer of the composite film.

The temperature dependence of Seebeck coefficient of the samples were measured and shown in Fig. 3. The absolute *S* value of the pristine thin film is 34.31 $\mu VK^{-1}$ at 300K and increases to 215.19 $\mu VK^{-1}$ when the temperature increased to 423 K. Significantly, the absolute *S* value of the hybrid thin film is 156.12 $\mu VK^{-1}$ at 303 K which is about 4 times higher than that of the pristine sample. It has an increasing trend with increasing temperature and achieves to a very high value of 239.26 $\mu VK^{-1}$ at 423 K. Based on the microstructure analysis, such enhancement of Seebeck coefficient can be explained to be the energy-filtering effect, causing by the nanoscale cluster of inorganic/organic composited. As the schematic diagram shown in Fig. 3, the band bending at inorganic/organic composited interface induces an energy potential barrier ($\Delta E$). When the energy of carriers higher than $\Delta E$, those higher part of carriers allowed passing the barrier while those with the energy of $\Delta E$ can be impeded. That acts as an energy filter for low energy electrons, thus filtered carriers with higher average energy can contribute to the enhanced Seebeck coefficient [37-39]. This result can also be confirmed from the hall measurements listed in Table 1. The carrier concentration decreases after $CH_3CH_3I$ hybrid due to the higher electrons scattered, but higher carrier mobility is obtained, which is commonly

reported in many inorganic-organic composited [32, 42].

Fig. 4(a) and 4(b) show the electrical conductivity and calculated power factor of thin films as the function of temperature. The electrical conductivity of the pristine is at 5.67× $10^4$ $Sm^{-1}$ at 303K and decreases to 4.46 × $10^4$ $Sm^{-1}$ after organic component hybrid due to the decrease of carrier concentration as we mentioned above. With the temperature raised, the electrical conductivity value of both the pristine and hybrid films was decreased. As a comprehensive result, the power factor has greatly increases from 0.07 $mWm^{-1}K^{-2}$ to 1.09 $mWm^{-1}K^{-2}$ at 303K, while the maximum *PF* is 1.72 $mWm^{-1}K^{-2}$ at 423K. To further investigate the influence of the thin film's thermal property, the room-temperature total thermal conductivity was measured by transient hot-wires theory method [31]. The temperature dependence of *ZT* value was calculated by using the power factor with a constant room temperature 303K. As shown in Fig. 4 (c), the total $\kappa$ of $Sb_2Te_3$ and $Sb_2Te_3/CH_3NH_3I$ composite thin films is 1.25 $Wm^{-1}K^{-1}$, and 0.68 $Wm^{-1}K^{-1}$, respectively. Due to the drastic scattering effect of heat-carrying phonons by the $CH_3NH_3I$ introduced, and the existence of nano-components formed by organic functional groups, the thermal conductivity value is lower. The point defects, including vacancies and $I^-$ interstitials, cause high-frequency phonons to scatter. In addition to, grain boundaries or phase boundaries also can lead to medium-frequency to low-frequency phonons scatter [41-43]. As Fig. 4(d) shown, the inorganic/organic $Sb_2Te_3/CH_3NH_3I$ interfaces and defects, with different crystal lattice configurations and associated local interfacial relaxation mechanisms caused this result [44, 45]. Therefore thermal conductivities of the composite thin films were significantly reduced. Phonons scattering enhancement is due to interface defects, which can significantly enhance the phonon scattering. It is indicated that such inorganic/organic $Sb_2Te_3/CH_3NH_3I$ interfaces and defects will have significant influence on phonon scattering. Consequently, thermal conductivity $\kappa$ is remarkably reduced, which contributes to the high *ZT*. The maximum *ZT* value 0.77 can be obtained at 423 K. Therefore, we conclude that the thermoelectric property of thermoelectric thin film is improved effectively by $Sb_2Te_3/CH_3NH_3I$ composite thin film and organic–inorganic composite thin films are a promising research direction of

thermoelectric materials.

In conclusion, the $Sb_2Te_3$ and $Sb_2Te_3/CH_3NH_3I$ composite thin films were prepared by thermal evaporation. Microstructural properties evolution and the corresponding thermoelectric properties of those thin films were studied and analyzed. Various characterization methods of SEM, TEM, EDS, XRD and Raman have been used to more directly confirmed that the mechanism of action of microstructure $Sb_2Te_3/CH_3NH_3I$ composite thin films. Inference of possibility is that the increasing mobility due to the energy-filtering effect, causing by the nanoscale cluster of inorganic/organic composited, and inorganic/organic $Sb_2Te_3/CH_3NH_3I$ interfaces and defects, besides, leads to improving the thermoelectric property of the $Sb_2Te_3$ nanocrystal thin film. In addition that the thermal conductivities of the composite thin films were significantly reduced, that prompt the *ZT* value greatly elevated to 0.77, which is about 100% enhancement.

**Acknowledgments** M. Wei and T. B. Chen contributed equally. This work is supported by the National Natural Science Foundation of China (No. 11604212), and Shenzhen Key Lab Fund (ZDSYS 20170228105421966).

**References**

[1] G. Chhatrasal, K. K. Kamal, Mater. Sci. 83 (2016), 330.

[2] X. Hu, Z. Huang, X. Zhou, P. Li, Y. Wang, Z. Huang, M. Su, W. Ren, F. Li, M. Li, Y. Chen, Y. Song, Adv. Mater. 29 (2017), 1703-236.

[3] J. J. Feng, W. Zhu, Y. Deng, Chin. Phys. B. 27, 4 (2018), 047210.

[4] C. C. Li, F. X. Jiang, C. C. Liu, P. P. Liu, J. K. Xu, Appl. Mater. Today. 15 (2019), 543-557.

[5] C. Gayner, Y. Amouyal, Adv. Funct. Mater. 2019, 1901789.

[6] Y. S. Hu, G. Yang, Z. Y. Tian, Z. Y. Hu, J. Alloys Comp. 790 (2019), 723-731.

[7] J. R. Sootsman, H. Kong, C. Uher, J. J. D'Angelo, C. I. Wu, T. P. Hogan, T. Caillat, M. G. Kanatzidis, Angew. Chem. Int. Ed. 47 (2008), 8618-8622.

[8] X. L. Su, P. Wei, H. Li, W. Liu, Y. Yan, P. Li, C. Su, C. Xie, W. Zhao, P. Zhai, Q.

Zhang, X. Tang and C. Uher, Adv. Mater. 29 ( 2017), 1602013.

[9] J. P. A. Makongo, D. K. Misra, X. Zhou, A. Pant, M. R. Shabetai, X. Su, C. Uher, K. L. Stokes, P. F. P. Poudeu, J. Am. Chem. Soc. 133 (2011), 18843.

[10] C. L. Wan, R. M. Tian, M. Kondou, R. G. Yang, P. G. Zong, K. Koumoto, Nat. Commun. 8 (2017), 1024.

[11] L. M. Wang, Z. M. Zhang, Y. C. Liu, B. R. Wang, L. Fang, J. J. Qiu, K. Zhang, S. R. Wang, Nat. Commun. 9 (2018), 3817.

[12] G. Chen, W. Xu, D. Zhu, J. Mater. Chem. C. 5 (2017), 4350-4360.

[13] N. W. Park, W. Y. Lee, J. E. Hong, T. H. Park, S. G. Yoon, H. Im, H. S. Kim, S. K. Lee, Nano. Res. Lett. 10 (2015), 1-9.

[14] G. C. Sosso, S. Caravati, M. Bernasconi, J. Phys. Condens. Matter. 21 (2009), 095410.

[15] Z. H. Zheng, F. Li, J. T. Luo, G. X. Liang, H. L. Ma, X. H. Zhang, P. Fan, J. Alloys Compd. 732 (2018), 958-962.

[16] L. Li, G. Li, T. Y. Zhang, C. G. Lin, G. X. Wang, S. X. Dai, Q. H. Nie, Q. Jiao, Cer. Inter. 43 (2017), 4508-4512.

[17] A. T. Duong, D. L. Nguyen, M. N. Nguyen, T. M. H. Nguyen, A. D. Nguyen, A. T. Pham, F. Ullah, Z. Tahir, Y. S. Kim, D. Q. Trung, Mater. Res. Exp. 6 (2019).

[18] J. J. Feng, W. Zhu, Y. Deng, Q. S. Song, Q. Q. Zhang, Appl. Energy Mater. 4 (2019), 2828-2836.

[19] N. Hatsuta, D. Takemori, M. Takashiri, J. Alloys Compd. 685 (2016), 147-152.

[20] C. Lin, C. Rüssel, S. Dai, Prog. Mater. Sci. 93 (2018), 1-44.

[21] N. Hatsuta, D. Takemori, M. Takashiri, J. Alloys Compd. 685 (2016), 147-152.

[22] M. Hong, J. Zou, and Z. G. Chen, Adv. Mater., 31 (2019), 1807071.

[23] K. H. Lim, K. W. Wong, D. Cadavid, Y. Liu, Y. Zhang, A. Cabot, K. M. Ng, Comp. Part B. 164 (2019), 54-60.

[24] C. Wan, R. Tian, M. Kondou, R. Yang, P. Zong, K. Koumoto, Nat. Commun. 8 (2017), 1.

[25] Z. G. Chen, X. L. Shi, L. D. Zhao, J. Zou, Prog. Mater. Sci., 97 (2018) 283-346.

[26] H. Ju, J. Kim, Nano, 10 (2016), 5730-5739.

[27] L. M. Wang, Y. C. Liu, Z. M. Zhang, B. R, Wang, J. J. Qiu, D. Hui, S. Wang, Compos B Eng. 122 (2017), 145–55.

[28] G. Wang, A. Lotnyk, C. Li, X. Shen, Scrip. Mater. 157 (2018), 115-119.

[29] E. J. Bae, Y. H. Kang, K. S. Jang, S. Y. Cho, Sci. Rep. 6 (2016), 18805.

[30] G. Chen, W. Xu, D. Zhu, J Mater Chem C. 5 (2017), 4350-4360.

[31] J. Z. Chen, Y. G. Rong, A. Y. Mei, Y. L. Xiong, T. F. Liu, Y. S. Sheng, P. Jiang, L. Hong, Y. J. Guan, X. T. Zhu, X. M. Hou, M. Duan, J. Q. Zhao, X. Li, H. W. Han, Adv. Energy Mater. 6 (2016), 1502009.

[32] K. Chatterjee, M. Mitra, K. Kargupta, S. Ganguly, D. Banerjee, Synthesis, Nanotechnology. 24 (2013), 215703

[33] M. Liu, M. B. Johnston, H. J. Snaith, Nature. 501 (2013), 395-398.

[34] G. C. Sosso, S. Caravati, and M. Bernasconi, J. Phys.: Condens. Matter. 21 (2009), 095410.

[35] W. Richter, A. Krost, U. Nowak, E. Anastassakis, Z. Phys. B - Condensed Matter. 49 (1982), 191-198.

[36] B. Park, S. M. Jain, X. Zhang, A. Hagfeldt, G. Boschloo, T. Edvinsson, ACS Nano. 9 (2015), 2088-2101.

[37] Y. Wang, L. Yang, X. L. Shi, X. Shi, L. D. Chen, Matthew S. Dargusch, J. Zou, Z. G. Chen, Adv. Mater. 31 (2019), 1807916.

[38] M. Tan, W. D. Liu, X. L. Shi, H. Gao, H. Li, C. Li, X. B. Liu, Y. Deng, Z. G. Chen, Small Methods. 3 (2019), 1900582.

[39] J. P. A. Makongo, D. K. Misra, X. Y. Zhou, A. Pant, M. R. Shabetai, X. L. Su, C. Uher, K. L. Stokes, P. F. P. Poudeu, J. Am. Chem. Soc. 133 (2011), 18843–18852.

[40] X. Mettan, R. Pisoni, P. Matus, A. Pisoni, J. Jacimovic, B. Nafradi, M. Spina, D. Pavuna, L. Forro, E. Horvath, J Phys Chem C. 119 (2015), 11506-11510.

[41] N. E. Coates , S. K. Yee , B. McCulloch, K. C. See, A. Majumdar, R. A. Segalman, J. J. Urban, Adv. Mater. 25 (2013), 1629-1633.

[42] W. Kim, J. Zide, A. Gossard, D. Klenov, S. Stemmer, A. Shakouri, A. Majumdar, Phys. Rev. Lett. 96 (2006), 045901.

[43] Y. Yu, C. J. Zhou, S. Y. Zhang, M. Zhu, M. Wuttig, C. Scheu, D. Raabe, G. J.

Snyder, B. Gault, O. Cojocaru-Mirédin, Mater. Today. 2019.

[44] L. Yang, Z. G. Chen, M. Hong, G. Han, J. Zou, ACS Appl. Mater. Interfaces. 7 (2015), 23694−23699.

[45] S. H. Lo, J. Q. He, K. Biswas, M. G. Kanatzidis, V. P. Dravid, Adv. Funct. Mater. 22 (2012), 5175-5184.

Figure(s)

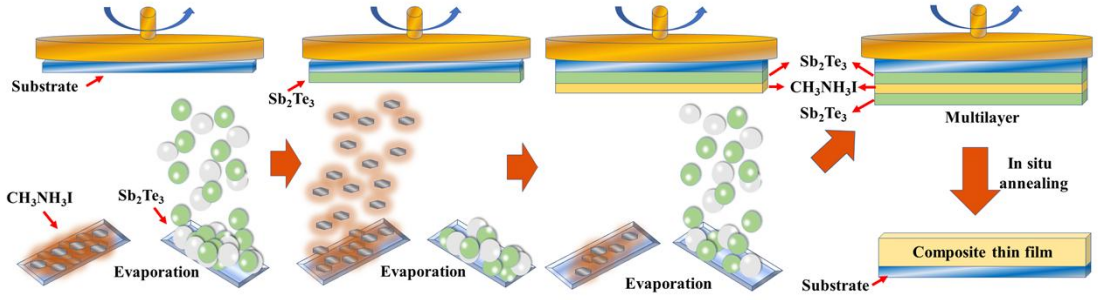


Fig.1 The schematic of preparing process

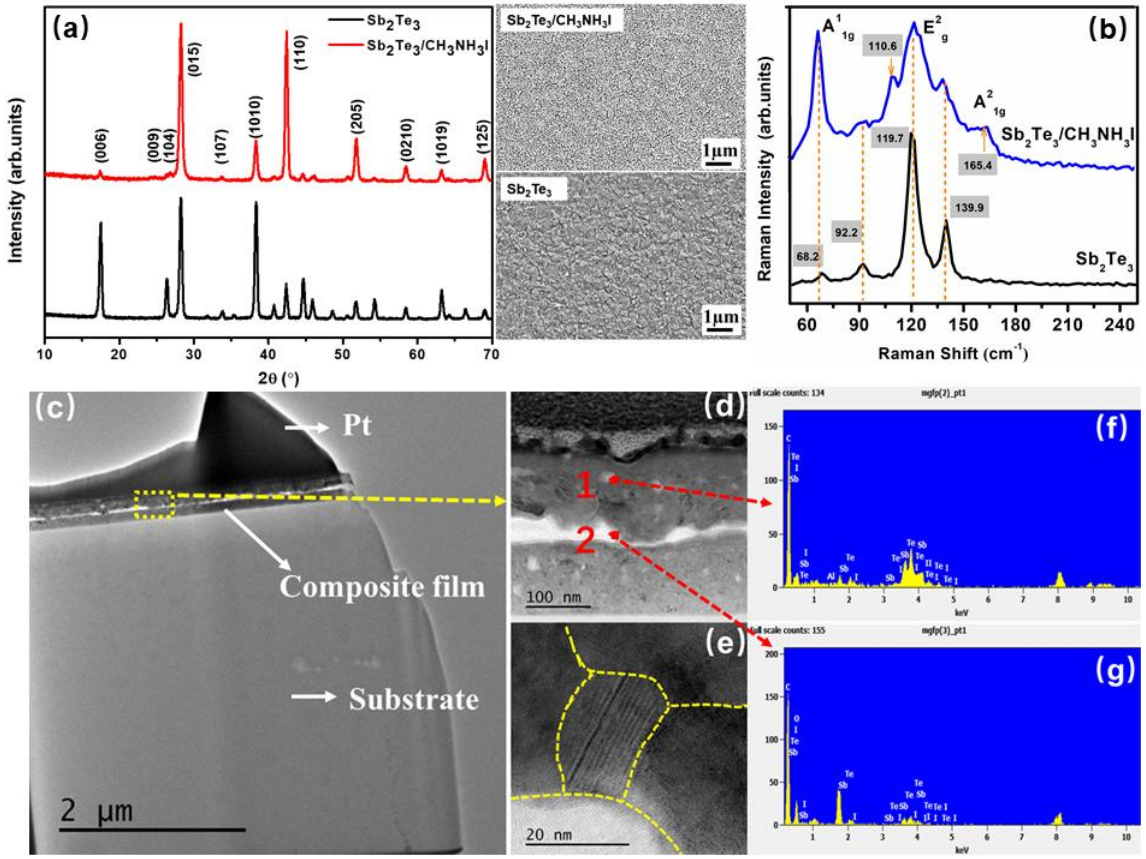


Fig. 2 (a) The XRD and SEM images of $Sb_2Te_3$ and $Sb_2Te_3/CH_3NH_3I$ composite thin films. (b) Raman measurements performed on $Sb_2Te_3$ and $Sb_2Te_3/CH_3NH_3I$ composite thin films, (c) TEM images observed from the cross section of $Sb_2Te_3/CH_3NH_3I$ composite thin film sample. (d) Pattern taken from yellow circle region in (c). (e) HRTEM image of $Sb_2Te_3/CH_3NH_3I$ composite thin film. (f), (e) Full scale counts patterns which were point 1 and 2 from (d)

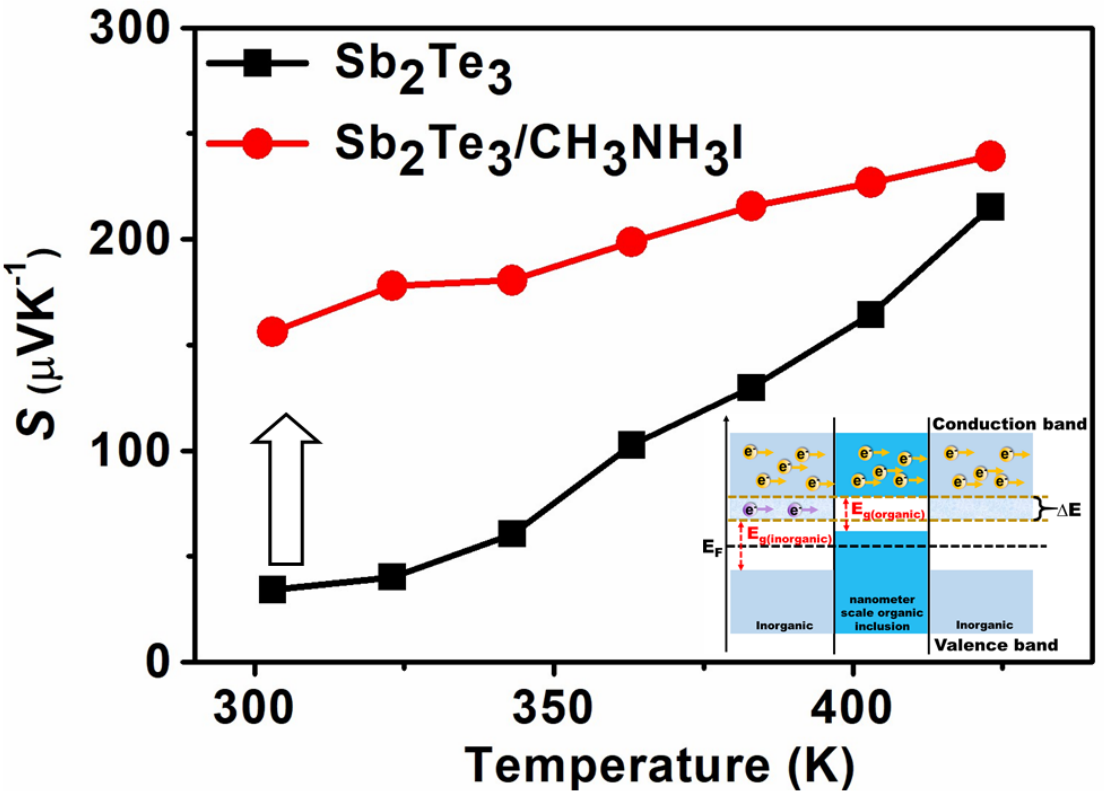


Fig. 3 Seebeck coefficient as a function of temperature for the $Sb_2Te_3$ thin film and $Sb_2Te_3/CH_3NH_3I$ composite thin film. And schematic illustration of the energy-filtering effect at the interface of inorganic/organic $Sb_2Te_3/CH_3NH_3I$ composite thin film inserted in

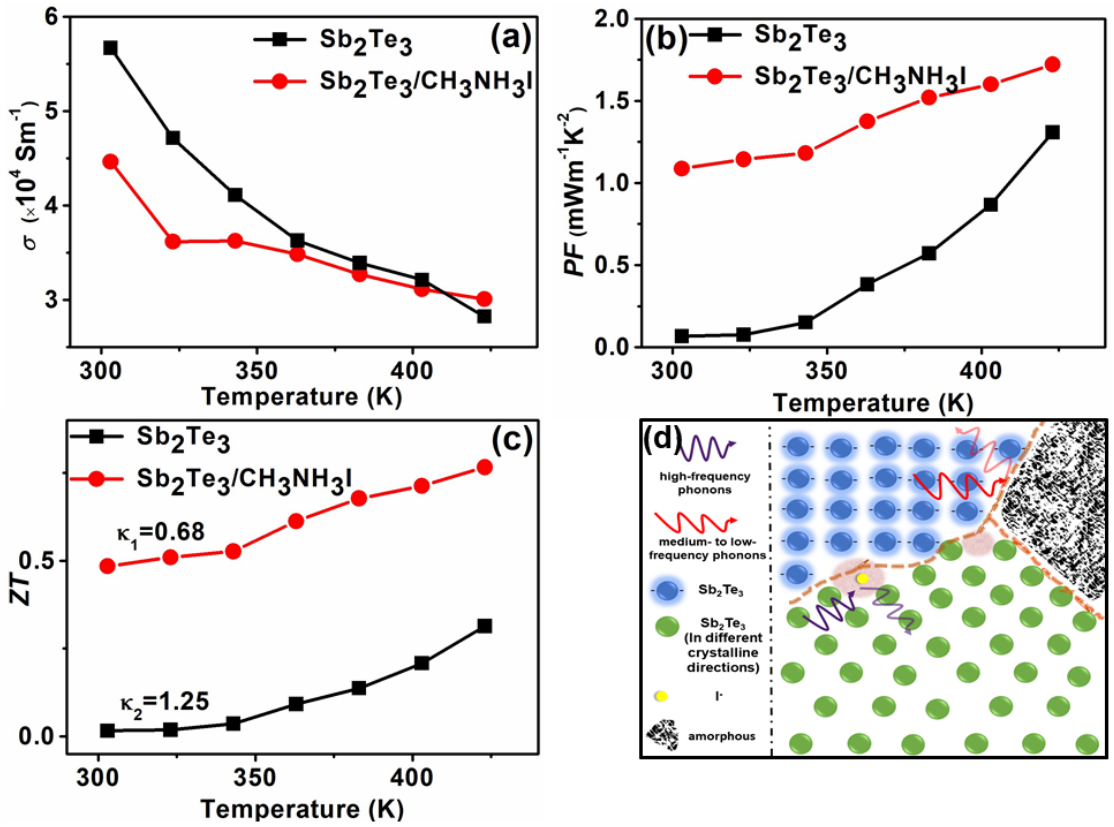


Fig. 4 Electrical transport properties as a function of temperature for all the films; (a) electrical conductivity, (b) power factor, (c) ZT values, (d) the various phonon scattering mechanisms for the samples of $Sb_2Te_3$ and $Sb_2Te_3/CH_3NH_3I$ composite thin films

**Table(s)**

Table 1 Actual contents，carrier mobility and concentration of thin films

| Sample | Sb (at.%) | Te (at.%) | I (at.%) | μ($cm^2V^{-1}s^{-1}$) | n ($cm^{-3}$) |
|---|---|---|---|---|---|
| $Sb_2Te_3$ | 40.07 | 59.93 | 0 | 85.7 | $1.52\times10^{19}$ |
| $Sb_2Te_3/CH_3NH_3I$ | 42.18 | 57.29 | 0.53 | 124 | $1.01\times10^{19}$ |